

Small-angle neutron scattering study of the role of feedstock particle size on the microstructural behavior of plasma-sprayed yttria-stabilized zirconia deposits

Hacène Boukari

National Institute of Standards and Technology, Gaithersburg, Maryland 20899, and Chemical Engineering Department, University of Maryland, College Park, Maryland 20742

Andrew J. Allen, Gabrielle G. Long, Jan Ilavsky, and Jay S. Wallace
National Institute of Standards and Technology, Gaithersburg, Maryland 20899

Christopher C. Berndt and Herbert Herman
Center for Plasma Spray, University of Stony Brook, New York 11794

(Received 16 September 2002; accepted 9 December 2002)

The microstructures of thick plasma-sprayed yttria-stabilized zirconia (8% mass fraction yttria) deposits were studied in a series of Porod small-angle neutron scattering (SANS) and multiple small-angle neutron scattering (MSANS) experiments. Three main void components were identified in the deposits: intrasplat cracks, interlamellar planar pores, and globular pores. The SANS and MSANS measurements were analyzed using the traditional theory for Porod scattering and a recently developed three-component model for MSANS evaluation. The average size, volume fraction, internal surface area, and orientation distribution for each void component within the deposits were determined. This study focused on gaining a better understanding of the effects of initial feedstock particle size and annealing temperatures on the microstructure of deposits sprayed under equivalent particle-impact conditions. Quantitative results are presented for each of four deposit samples: one prepared using the as-received feedstock particle wide-size distribution and three prepared from feedstock powder of different and relatively narrow particle size ranges with average sizes of 32, 47, and 88 μm . Except for the coarse (88 μm) feedstock powder, only mild monotonic variations were found in the **microstructural** anisotropies, the porosities ($13 \pm 1\%$), and the internal surface areas in the as-sprayed deposits. The internal surface area was independent of the feedstock particle size, even with the coarse feedstock. When the deposits were annealed at high temperatures (1100 and 1400 $^{\circ}\text{C}$), the microstructures were altered with a reduction of the total internal surface area and a mild coarsening of the voids. These changes in the microstructural evolution were well-captured and described by the three-component model. The results were compared and related with those obtained from scanning electron microscopy images and elastic moduli measurements.

I. INTRODUCTION

Small-angle neutron scattering (SANS) and electron microscopy investigations have indicated that the microstructure of plasma-sprayed ceramic deposits consists mainly of three different types of voids: interlamellar planar pores, intrasplat cracks, and globular pores.¹ Characterizing the nature of these voids is of practical importance since the mechanical and thermal properties of the deposits depend strongly on the microstructure. Correlating the variations in the properties with those of the microstructure can thus provide a basis for optimal design and fabrication of deposits for different applications.

Plasma-sprayed deposits are prepared by spraying molten or partially molten feedstock particles onto a solid substrate. Upon rapid solidification and cooling, the particles form a complex structure composed of solid

splats or lamellae separated by interlamellar pores. As shown in Fig. 1, cracks as well as globular voids appear inside the lamellae and are likely due to rapid solidification of the molten particles. The resultant structure depends on a number of processing parameters whose influence on the microstructure needs to be systematically investigated. Understanding this dependence may lead to a better predictability of the deposit microstructure and, more importantly, to the capability to tailor the properties of these materials for specific applications.

Recently, some of the present authors described the results of a systematic investigation of the influence of spray angle on several plasma-sprayed deposits.¹ In the present paper, we describe new results of a series of experiments aimed at investigating the role of the size of the feedstock powder particles on the microstructure of the deposits. For this purpose, a single batch of **sph-**

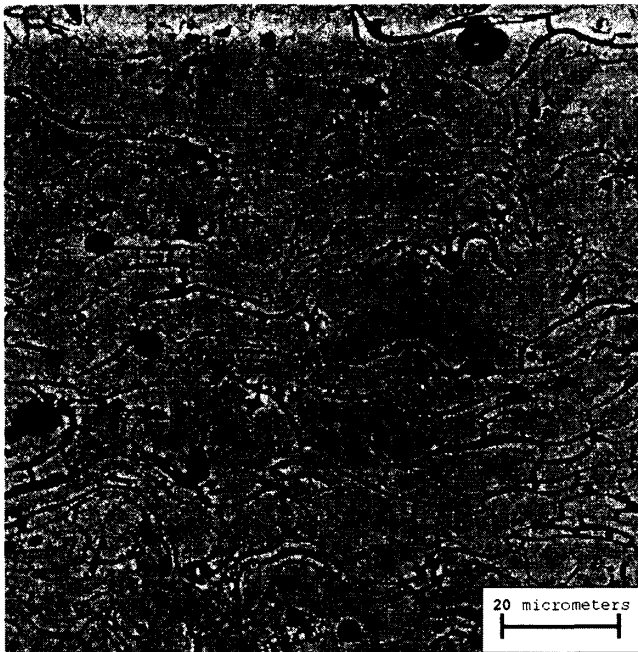


FIG. 1. Electron micrograph of the microstructure of the cross section of a YSZ deposit sprayed with the fine Metco powder.

roidized feedstock powder (Sulzer-Metco, Troy, MI) was used: yttria-stabilized (8% mass fraction) zirconia (YSZ) with a number-weighted mean particle size of $56\ \mu\text{m}$. By differential sieving, three powder subpopulations were derived from this original as-received powder with number-weighted mean particle size: 32 , 47 , and $88\ \mu\text{m}$. Thus, four deposits, derived from four different feedstocks, were sprayed and studied: fine ($32\ \mu\text{m}$), medium ($47\ \mu\text{m}$), ensemble or as-received ($56\ \mu\text{m}$), and coarse ($88\ \mu\text{m}$). For a consistent comparison, appropriate spray conditions were selected to give the same impact temperature ($2790\ ^\circ\text{C}$) and the same spread of the particles for each of the four deposits.

The focus of the study is threefold: to characterize the microstructure of the four deposits, determine the effect of heat treatment on each microstructure, and relate associated changes in the microstructure to those in the elastic modulus. For this purpose, three different measurements were obtained. First, SANS, multiple small-angle neutron scattering (MSANS), and scanning electron microscopy (SEM) were applied to characterize the bulk and surface microstructure of the deposits. Second, the porosity of the deposits were determined from high-precision density measurements. Finally, companion Hertzian indentation experiments were performed to determine the elastic moduli of the deposits.

In the SANS analysis, the internal surface area of the deposits was extracted by fitting the SANS data with the usual Porod's law.²⁻⁴ The MSANS data were analyzed with a 3-component void model to break down the total porosity and internal surface area into its main in-

dividual void-components, namely the interlamellar voids, the intrasplat cracks, and the globular pores.⁵ This model was developed specifically for these deposits to take into account their anisotropic microstructure by assuming two different anisotropic spheroidal void networks and a population of globular (spherical) voids to represent the actual void-space in the material. It is assumed that the spheroidal void networks permeate and fill, as closely as possible, the actual void volumes they represent. The results of this analysis indicate that this simple model captures the essential features of the complex microstructure of the actual deposits. In particular, the dominant contribution to both SANS and MSANS data is associated with a spheroid/void orientation where the scattering is most characteristic of the (short) mean opening dimension of the spheroid or planar void, the physical dimension of interest here. The results are found to be consistent with the observations from SEM images and account for the changes in the microstructure caused by heat treatment.

In what follows, we describe the measurements and the results of the data analysis. In Sec. II, we present the details of the processing parameters and conditions used to spray the Metco deposits. Then we present the density, SANS, and MSANS measurements for the different deposits in Sec. III. Remarkably, we show that the total porosity varies monotonically with the size of the feedstock particles. Meanwhile, the internal surface area is almost constant, independent of the size of the particle. In Sec. III. B. 2, we detail the results of the MSANS analysis and correlate them with the observations of the SEM images. In Sec. III. C, we describe the measurements of the elastic modulus performed on two samples at different heat-treatment conditions and relate them to the parameters derived from the MSANS measurements. Finally, in Sec. IV we discuss the results and show that, under similar spray conditions, the size of the feedstock particle has a surprisingly mild effect on the microstructure of the deposits, a conclusion of significance in setting the specifications for the spray parameters.

II. SAMPLE PREPARATION

The YSZ (8% mass fraction yttria) powder with low silica content (below 0.1% mass fraction), which was plasma-spheroidized, was acquired from Sulzer-Metco (batches AE 7590 to AE 7593). The as-received $56\text{-}\mu\text{m}$ mean particle-size powder was sieved into three feedstocks of different sizes [fine ($37\ \mu\text{m}$), medium ($47\ \mu\text{m}$), and coarse ($88\ \mu\text{m}$)]. The deposits were sprayed at the Center for Plasma Spray at Stony Brook University, New York, using a Metco 9MB torch (Sulzer Metco, Troy, MI) with a Metco GH nozzle and Metco #2 powder feeder. The spray gun parameters were selected and adjusted so that the average impact temperature ($2790\ ^\circ\text{C}$),

particle feed rate, and spread of the impacting particles on the substrates were reasonably the same for all feedstocks. An in-flight pyrometer IPP2000 was used with a remote iris (Inflight Ltd., Idaho Falls, ID) together with an in-flight trajectory sensor (Intelligent Spray Sensor 1024 by Inflight Ltd.) to measure these parameters. Thus, the spray parameters were varied to maintain the same physical deposition conditions and, hence, separate out feedstock profile size as the sole deposition variable. The final spray parameters are listed in Table I.

Thick samples were fabricated by making numerous passes of the spraying torch (290 to 350 passes depending on the particle size). During spraying, the surface temperature of the samples was monitored with a handheld infrared thermometer. The surface temperature was maintained relatively constant (170–230 °C) by blowing compressed air on the samples. To obtain free standing samples, a 70- μm aluminum bond coat was deposited on the substrate before spraying the powder and was later dissolved with hydrochloric acid. Finally, tetragonal-shaped pieces were precision cut from each original bulk deposit with a standard diamond saw to provide suitable samples for accurate density values.

To study the effect of heat treatment on the microstructure a section of each deposit was placed in a temperature-controlled furnace. Two target temperatures were used, 1100 and 1400 °C, and the dwell time was set to 1 h. The effect of thermal cycling on the microstructure was also studied by subjecting a section of each deposit to temperature cycles (10 \times) between room temperature and 1100 °C with a 30-min dwell time in the furnace at 1100 °C. The heating and cooling rates were set at 600 °C/h during the heat treatment. Thus, for each feedstock size (fine, medium, coarse, and ensemble) four conditions were studied: as-sprayed, heat treated at 1100 °C for 1 h, heat treated at 1400 °C for 1 h, and thermally-cycled (10 \times) between room temperature and 1100 °C. In all, a total of 16 different samples were characterized and studied. All measurements (SANS, MSANS, SEM, density, and elastic modulus) were performed *ex situ* after thermal treatment in each case. More detailed information about the studied deposits is listed in Table II.

TABLE I. Spray processing conditions.

| Powder type | Ensemble | Fine | Medium | Coarse |
|--|----------|-------|--------|--------|
| Power (kW) | 33.2 | 33.1 | 37.2 | 45.6 |
| Current (A) | 550 | 500 | 550 | 600 |
| Voltage (V) | 65.8 | 66.2 | 76.2 | 76 |
| Argon $\times 10^{-3}$ (m ³ /s) ^a | 0.67 | 0.67 | 0.67 | 0.67 |
| Hydrogen $\times 10^{-3}$ (m ³ /s) ^a | 0.1 | 0.1 | 0.1167 | 0.183 |
| Feed. rate Argon $\times 10^{-6}$ (m ³ /s) ^a | 75 | 66.67 | 62.5 | 70.83 |
| Feed. rate powder $\times 10^{-4}$ (kg/s) | 4.167 | 4.167 | 4.167 | 4.167 |

^aRate of the plasma gases measured at standard pressure and temperature.

III. EXPERIMENTS

A. Density–porosity measurements

Rectangular parallelepiped samples of nominal dimensions (5 mm \times 5 mm \times sprayed-thickness 3.5 mm) were diamond cut from the bulk as-sprayed deposits and then ground to smooth the surface. Their orthogonal dimensions were measured with a micrometer screw-gauge to a standard precision of $\pm 1 \mu\text{m}$. The mass of each sample was then determined with a high-precision balance (± 0.001 g). The porosity value of each sample was calculated using a theoretical density of YSZ, $\rho_d = 6 \text{ g/cm}^3$. The density values represent the averages over several (>5) independent measurements, giving 0.2% relative standard deviations. In Fig. 2, the changes in the total porosities are given as a function of the mean size of the feedstock for all 16 deposits. Note that the sample porosity increases with the mean powder size and that heat treatment reduces the sample porosity by annealing out some of the voids. In Table II, we include the values of the density and porosity of the different samples as well as the values of the internal surface area.

B. SANS and MSANS measurements

The SANS and MSANS experiments were carried out at the 8m SANS instrument at the Center for Neutron Research at the National Institute of Standards and Technology in Gaithersburg, Maryland. Details on the 8m SANS instrument are described elsewhere.⁶ The experiments consist of measuring the intensity of the neutrons scattered by the sample at small angles ($< 7^\circ$) away from the forward direction of the incident beam. For this purpose, a beam of neutrons of wavelength λ was directed toward the sample after passing through several collimating apertures. For the SANS experiments we used $\lambda = 0.6 \text{ nm}$, which is appropriate for Porod scattering and the determination of the internal surface area of the sample. The objective in MSANS experiments is to determine the broadening of the scattering profiles as a function of the neutron wavelength.^{7,8} Thus, scattering profiles from each deposit were systematically collected at five different wavelengths: 1.0, 1.2, 1.4, 1.6, and 1.8 nm. The scattered neutrons from the sample were collected by a two-dimensional proportional detector located 3.6 m away from the sample. Typically, every two-dimensional scattering distribution was measured over a 20–30 min period to ensure good statistics in the scattering distribution. The data were further reduced to yield intensity versus the amplitude of the scattering wavevector defined by $q = 4\pi/\lambda \sin(\theta/2)$, where θ is the scattering angle.

1. SANS measurements

Unlike many porous microstructures, plasma-sprayed deposits show anisotropy in the orientation distribution of the various void components. Previous investigations

on similar deposits have shown that the intrasplat cracks are preferentially oriented along the spray direction (perpendicular to the surface of the substrate) whereas the interlamellar pores tend to align parallel to the substrate.⁴ This observation was confirmed by SEM images such as that shown in Fig. 1.

A quantitative assessment of the microstructural anisotropy of the deposits is possible by collecting SANS

data under an appropriate configuration, in which the scattering wavevector q lies in a plane perpendicular to the substrate; i.e., the direction of the incident neutron beam is parallel to the substrate plane (perpendicular to the spray direction). The measured two-dimensional SANS data are then sector-averaged in 10° increments around the incident beam position on the detector to determine the angular intensity profile, $I(q, \phi)$, where ϕ

TABLE II. Information on the plasma-sprayed samples.

| Sample | Size (10^{-6} m) | Temperature ($^\circ$ C) | Thickness (10^{-3}) | Density (g/cm^3) | Porosity (%) | Surface area (m^2/cm^3) |
|----------|---------------------|---------------------------|-------------------------|----------------------|----------------|-----------------------------|
| Fine | 32 | as-sprayed | 3.57 ± 0.01 | 5.262 ± 0.002 | 12.3 ± 0.1 | 2.44 |
| Medium | 47 | as-sprayed | 3.58 ± 0.01 | 5.173 ± 0.002 | 13.8 ± 0.1 | 2.27 |
| Coarse | 88 | as-sprayed | 3.57 ± 0.01 | 4.854 ± 0.002 | 19.1 ± 0.1 | 2.39 |
| Ensemble | 56 | as-sprayed | 3.58 ± 0.01 | 5.132 ± 0.002 | 14.5 ± 0.1 | 2.30 |
| Fine | 32 | 1100 | 3.56 ± 0.01 | 5.295 ± 0.002 | 11.8 ± 0.1 | 1.92 |
| Medium | 47 | 1100 | 3.61 ± 0.01 | 5.182 ± 0.002 | 13.6 ± 0.1 | 1.96 |
| Coarse | 88 | 1100 | 3.56 ± 0.01 | 4.860 ± 0.002 | 19.0 ± 0.1 | 2.22 |
| Ensemble | 56 | 1100 | 3.53 ± 0.01 | 5.144 ± 0.002 | 14.3 ± 0.1 | 1.96 |
| Fine | 32 | 1400 | 3.33 ± 0.01 | 5.349 ± 0.002 | 10.8 ± 0.1 | 1.31 |
| Medium | 47 | 1400 | 3.48 ± 0.01 | 5.261 ± 0.002 | 12.3 ± 0.1 | 1.41 |
| Coarse | 88 | 1400 | 3.42 ± 0.01 | 4.961 ± 0.002 | 17.3 ± 0.1 | 1.50 |
| Ensemble | 56 | 1400 | 3.30 ± 0.01 | 5.222 ± 0.002 | 13.0 ± 0.1 | 1.37 |

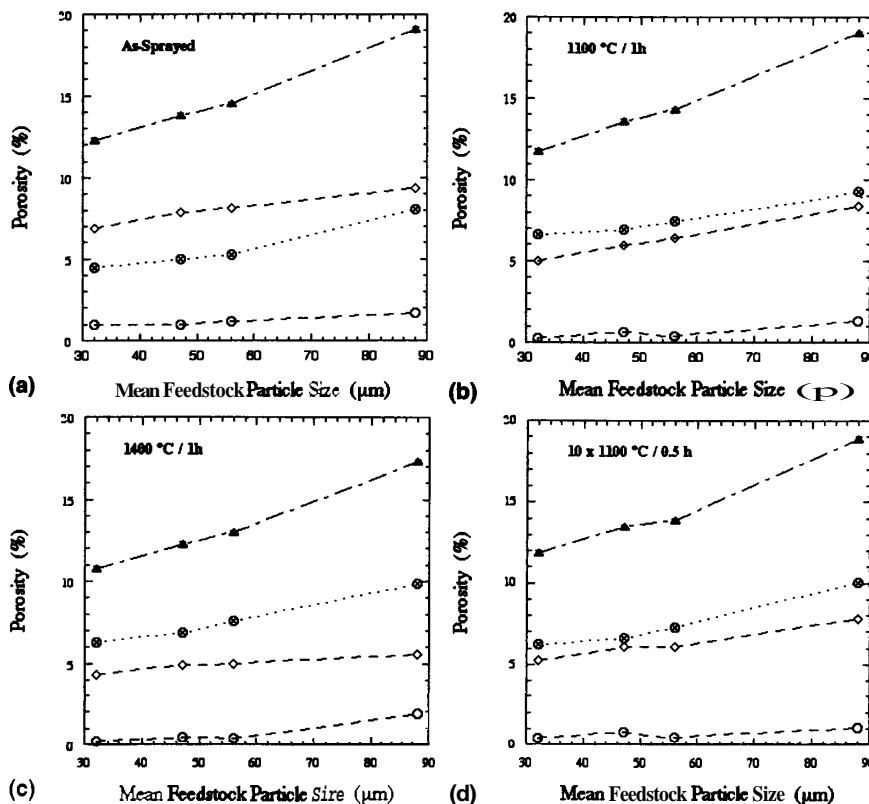


FIG. 2. (a-d) Measured porosities shown as a function of the mean size of the feedstock powder. The total porosity (A), determined from density measurements, is broken into its main contributors using the 3-component void model: (◇) intersplat voids, (⊗) globular voids, and (○) intrasplat cracks. Each figure is labeled with the annealing temperature. The error bars are two standard deviations in length (close to the size of the markers) and are shown on the measured total porosity only.

denotes the polar angle in the two-dimensional plane of the detector. The intensity profiles, $I(q, \phi)$ versus q , are analyzed to extract $S_v(\phi)$ defined as

$$I(q, \phi) = \frac{2\pi|\Delta\rho|^2}{q^4} S_v(\phi) \quad (1)$$

where $\Delta\rho$ is the difference in the scattering length density between that of the voids and that of the matrix ($\Delta\rho = 5.22 \times 10^{14} \text{ m}^{-2}$ for tetragonal zirconia, up to 5% more for YSZ depending on the exact crystalline phases present). The ϕ -dependence of $S(\phi)$ quantifies the scattering anisotropy of the sample. Further, the orientationally weighted average $\langle S_v(\theta) \rangle$ is calculated to be the total scattering surface area per unit volume and is the same as the theoretical value S_v defined in the following expression:

$$\langle I(q) \rangle = \frac{2\pi|\Delta\rho|^2}{q^4} S_v \quad (2)$$

where $\langle \dots \rangle$ implies an orientational average. In contrast to the common Porod equation,² Eq. (2) is applicable to a more general case of anisotropic microstructures as a three-dimensional average of the sample orientation is taken over all solid angles with respect to the direction of the wavevector q to take into account the anisotropic scattering of the samples.^{4,9}

Anisotropic SANS measurements were obtained using a 0.6-nm wavelength neutron beam and covered a q range between 0.1 and 1.6 nm^{-1} , sufficient to characterize the Porod region of scattering²¹ and to determine S_v . All measurements were corrected for background (air) and calibrated to absolute measurements using a silica standard. In Fig. 3 typical angular dependence of measured $S_v(\phi)$ are shown for the deposits made from the ensemble and coarse feedstocks. The anisotropic nature of the microstructure is apparent; there are substantial variations of S_v as a function of ϕ . Note that near $\phi = 0^\circ$, $S_v(\phi)$ is the internal surface area dominated by the projected surface area of the interlamellar pores that are parallel to the substrate plane, whereas near $\phi = 90^\circ$ $S_v(\phi)$ is the internal surface area dominated by the projected surface area of the intrasplat cracks that are oriented perpendicular to the substrate plane. In Fig. 3 are also plotted the $S_v(\phi)$ -values measured at different annealing conditions. Here one notices the reduction of the internal surface area as the annealing temperature is increased. However, it is difficult to determine directly from these data whether all or part of the void components are affected by such annealing.

Further insights into the role of feedstock can be drawn from Fig. 4, in which the angular average of the internal surface-area ($\langle S_v \rangle$) is plotted as a function of the mean

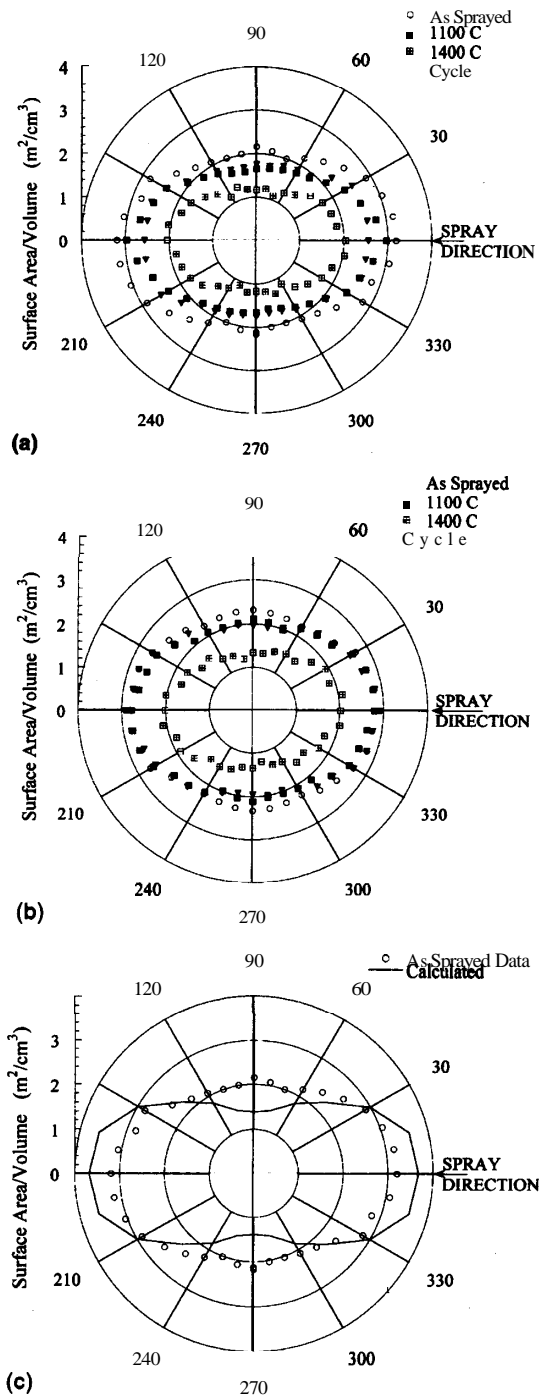


FIG. 3. The surface area of two different deposits made from (a) the ensemble and (b) the coarse feedstock powders is shown as a function of the angle on the two-dimensional detector at different annealing temperatures. The values are determined from the SANS measurements obtained from the sample, which is oriented along the asymmetrical axis with respect to the incident neutron beam (see text for details). The error bars are two standard deviations in length (close to the size of the markers). (c) The measured total surface area (○) of the deposit made from the ensemble feedstock is compared with the calculated one (—) as derived from analysis and fitting of the MSANS data with the 3-component void model (see text for details). For clarity, we show the anisotropic surface area of the nonannealed deposit (as-sprayed) only.

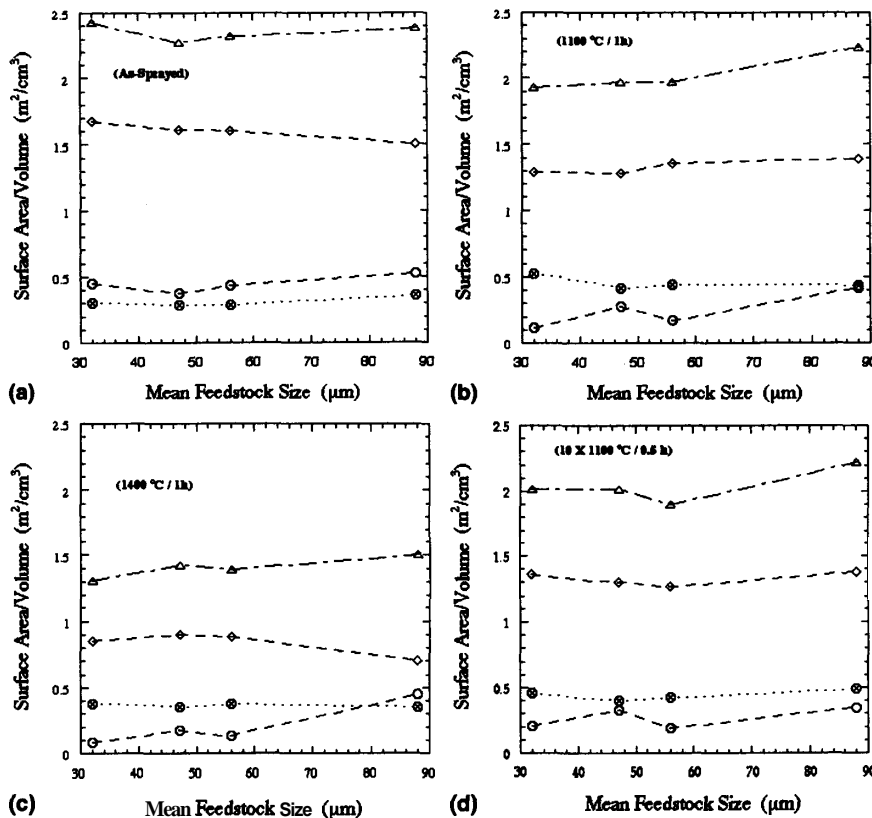


FIG. 4. (a-d) Surface areas are plotted as a function of the size of the feedstock powder. The total surface area (A), determined from Porod SANS measurements, is broken into the contributions of the three components: (\bullet) intersplat voids, (\otimes) globular pores, and (\circ) intrasplat cracks using the 3-component void model. The annealing temperature labels each plot.

size of the feedstock particles for different annealing conditions. Interestingly, the $\langle S_v \rangle$ values are nearly constant, independent of the feedstock particle size; variations in $\langle S_v \rangle$ values do not exceed 5%, well within the general precision of the SANS measurements. It is interesting to contrast these variations in the internal surface area (Fig. 4) with those of the porosity shown in Fig. 2. For the same annealing conditions $\langle S_v \rangle$ values do not vary significantly (<5%) while the porosity values vary by as much as 50%. Also, Fig. 4 shows that thermal cycling does not have a cumulative effect; the $\langle S_v \rangle$ values obtained from the deposit annealed once at 1100° for 1 h are within the experimental uncertainties similar to those obtained from the deposit thermally cycled between room temperature and 1100 °C several times (10x).

2. MSANS measurements

The MSANS formalism was developed to investigate large structures up to several micrometers in size, a size range not accessible by traditional SANS techniques.^{7,8} The assumption of the theory is that the incident neutrons are multiply scattered by the sample. While the individual scattering events are governed by coherent small-angle scattering theory, the multiple scattered events sum together incoherently. Provided there exists sufficient

multiple scattering events, the entire incident beam broadens as it passes through the sample. This condition is well satisfied by the thick samples—3.3–5.0 mm thick—which have a relatively large volume fraction of open or closed voids. A typical MSANS experiment consists of measuring the intensity profile as a function of the amplitude of the wave vector (q) of the scattering sample at different wavelengths of the incident neutron beam. The changes in the width of the measured intensity profiles are determined as a function of the wavelength and then analyzed using an MSANS model that describes appropriately the microstructure of the scattering sample. The anisotropy in the present samples provides an additional factor to take into account.^{5,9} For this purpose, the broadening of the intensity profile was measured as a function of the neutron wavelength using two sample orientations with respect to the direction of the incident neutron beam: (i) symmetric orientation, in which the beam direction is parallel to the spraying direction and the sample's surface facing the beam is that parallel to the substrate plane, and (ii) asymmetric orientation, in which the beam direction is parallel to the spraying direction, but the sample's surface facing the beam is that perpendicular to the substrate plane. Thus, two sets of MSANS data are generated and must be analyzed consistently using the MSANS model.

The MSANS data were collected using 1.0, 1.2, 1.4, 1.6, and 1.8 nm neutron wavelengths. The two-dimensional intensity distribution was radially averaged to derive the intensity profile I_c as a function of the amplitude of the wave vector q . Because the interest was in the broadening of the profile, there was no need to subtract the background and calibrate the data. Following Allen et al.⁹ a Gaussian function was used to fit the upper part of the measured profile, and the width of the profile r_c was deduced. The fitting range was limited to the intensity range between 40% and 90% of the maximum intensity at $q = 0$. Finally, for each wavelength, the measured width of the profile was corrected for the width associated with instrumental resolutions. In Fig. 5, as a typical example, the variations of the corrected width r_c are plotted as a function of the neutron wavelength for the sample made with fine feedstock. The two sets of r_c values were the basic data analyzed within the 3-component void model discussed below. To quantify the microstructural anisotropy, the MSANS measurements, obtained in the asymmetric orientation of the sample, were averaged over 15° sectors taken around the incident beam direction. The results are shown in Fig. 6. These MSANS data were used to check for consistency in the calculated anisotropy as derived from the 3-component void model.

Unlike isotropic microstructures, the anisotropy in the deposits presents both a challenge for exploiting the MSANS measurements to gain insight into the microstructure of the samples and an opportunity to separate the different anisotropic components. Recently, Allen et al. extended the MSANS formalism to include scattering from anisotropic particles.⁵ From this work, a specific 3-component void model was developed to

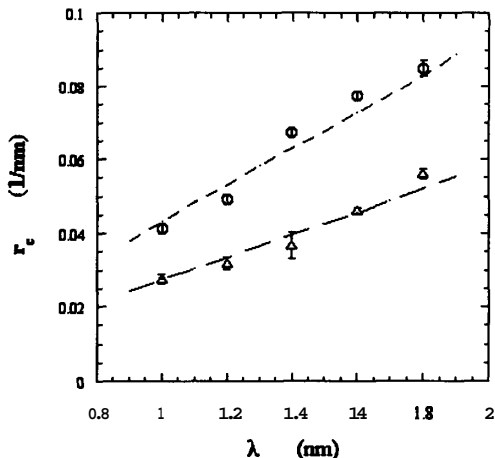


FIG. 5. The width of the MSANS intensity profile is shown as a function of the wavelength of the neutron beam: (O) for the symmetric orientation and (A) asymmetric orientation (see text for details). The error bars are two standard deviations in length determined from fitting the measured intensity profiles with a Gaussian function. The dashed lines are determined from fitting simultaneously the width measurements with the 3-component void model (see text).

investigate the particularities of thermal spray deposits.⁹ The model includes two anisotropic distributions of spheroidal voids of different radii and aspect ratios ($R_1, \beta_1 R_1$, and $R_2, R_2, \beta_2 R_2$) and one population of spherical pores of radius R_0 . These elements represent the intersplat voids, intrasplat cracks, and globular pores, respectively. β_1 and β_2 define the "oblateness" of the spheroids. The primary goal in the analysis is to calculate the appropriate volume fractions (ϕ_1, ϕ_2, ϕ_0), the surface areas (S_{v1}, S_{v2}, S_{v3}), the sizes (R_1, R_2, R_0), and the aspect ratios (β_1, β_2) of the component void elements. For consistency, these parameters must reproduce (i) the total

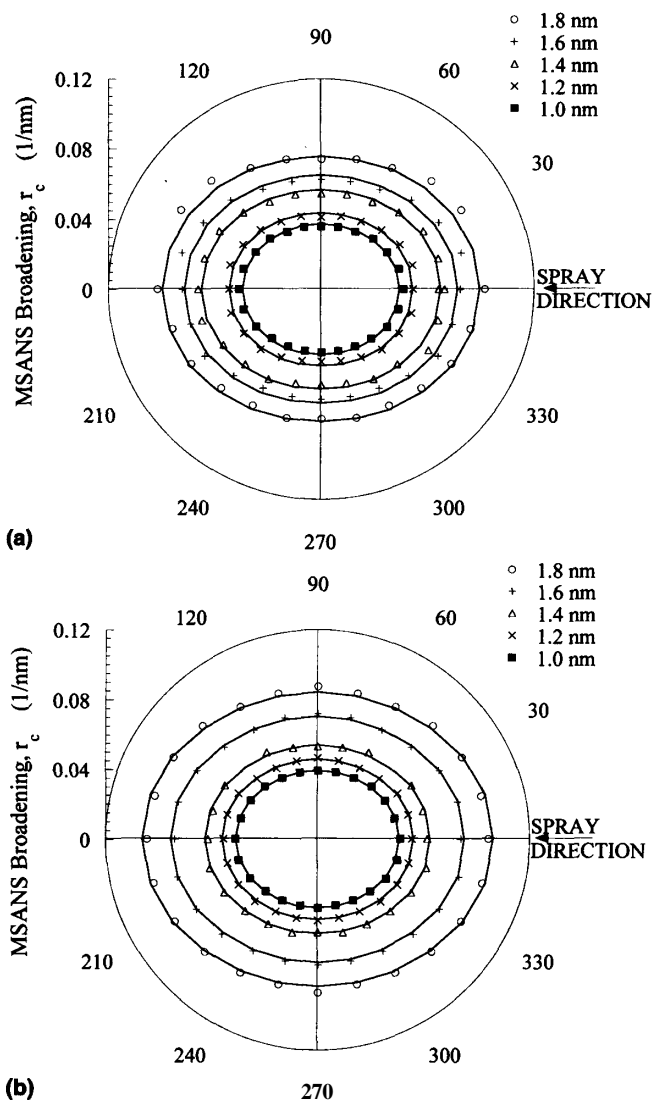


FIG. 6. The measured and calculated anisotropic MSANS broadening of the deposits made from the (a) ensemble and (b) the coarse feedstock powders (no thermal annealing) are plotted as a function of the angle defined in the two-dimensional detector. The measurements were collected at different neutron wavelengths as indicated in the figure. The vertical bars (close to the size of the markers) are two standard deviations in length determined from fitting the measured intensity profiles with a Gaussian function.

surface area S_v , determined from the SANS-data, (ii) the total porosity ϕ_T , derived from the density measurements, and (iii) the two sets of MSANS broadening measurements obtained with the two sample orientations. In addition, the angular orientation distribution of the spheroidal elements, combined with their concentration, must yield the observed MSANS anisotropy.

Despite the number of unknown parameters (17 in total), the constraints represent stringent requirements, thereby reducing the number of physically reasonable solutions. The experimental measurements were fitted using the 3-component void model. The model parameters were then adjusted with least-square refinement, yielding at the end, the volume fractions, sizes, specific surface areas, and orientation distributions with respect to the incident beam direction of all void components for each sample. Generally, it was found that $\beta_1 = 1/10$ and $\beta_2 = 1/5$ and $1.2 \leq R_0/R_1 = R_0/R_2 \leq 1.3$ gave good fits to all of the data. The relative volume fractions and the orientation distribution of the spheroidal components were, however, varied to account for the anisotropy. Table III lists the calculated values of the parameters for each deposit. Further, the variations of the calculated values of the parameters are included in different corresponding figures. In Figs. 2 and 4 are plotted, respectively, the calculated partial porosities and the calculated partial internal surface areas of each void-component at various annealing conditions for the different samples. Also, the calculated SANS and the MSANS anisotropies are included in Figs. 3(c) and 6, respectively. In Fig. 5 the calculated MSANS broadening is shown as a function of neutron wavelength. As an indicator of the changes in the size of the voids in the samples $2R_0$, the diameter of the globular pore is plotted against the feedstock particle size in Fig. 7.

C. Indentation measurements

The apparent elastic modulus of each sample was measured along the spray direction $E_{||}$ and in the substrate plane E_{\perp} using a modified commercial indentation instrument.¹⁰

TABLE III. Results of analysis of MSANS measurements based upon the 3-component void model.

| Sample | Temperature (°C) | R_0 ($\times 10^{-6}$ m) | R_1/R_0 | R_2/R_0 | ϕ_1/ϕ_0 (%) | ϕ_2/ϕ_0 (%) | ϕ_3/ϕ_0 (%) |
|----------|------------------|-----------------------------|-----------|-----------|---------------------|---------------------|---------------------|
| Fine | as-sprayed | 0.337 | 1 | 1.3 | 8 | 56 | 36 |
| Medium | as-sprayed | 0.400 | 1 | 1.3 | 7 | 57 | 36 |
| Coarse | as-sprayed | 0.510 | 1 | 1.3 | 9 | 49 | 42 |
| Ensemble | as-sprayed | 0.415 | 1 | 1.3 | 8 | 56 | 36 |
| Fine | 1100 | 0.315 | 1 | 1.2 | 2 | 42 | 56 |
| Medium | 1100 | 0.382 | 1 | 1.3 | 5 | 44 | 51 |
| Coarse | 1100 | 0.494 | 1 | 1.3 | 7 | 44 | 49 |
| Ensemble | 1100 | 0.389 | 1 | 1.3 | 3 | 45 | 52 |
| Fine | 1400 | 0.415 | 1 | 1.2 | 2 | 40 | 58 |
| Medium | 1400 | 0.447 | 1 | 1.3 | 4 | 40 | 56 |
| Coarse | 1400 | 0.648 | 1 | 1.3 | 11 | 32 | 57 |
| Ensemble | 1400 | 0.464 | 1 | 1.3 | 3 | 38.5 | 58.5 |

Indentation loading/unloading curves were recorded to a precision of ± 3 mN (0.3 g-force) and displacements to ± 10 nm. For indentations, a 2.381 mm ($3/32$ in.) diameter WC sphere and a nominal 4 N load were used, resulting in a contact diameter between the WC sphere and the sample of approximately 50 μm and a peak elastic penetration depth of approximately 2.5 μm . The apparent modulus of the sample E_a was determined from the load-displacement curve using the standard Hertzian contact theory that yields the following equation:¹¹

$$E_a = \left(\frac{9}{16}\right)^{1/2} P h^{3/2} R_1^{-1/2}, \quad (3)$$

where h is the depth of elastic penetration of the indenter, P the load, and R_1 the indenter radius.

A least-squares fit was performed of $P^{2/3}$ versus h with E_a as a fitting parameter. To determine the true modulus of the sample, a correction was made for the elastic properties of the spherical indenter using the following formula:

$$E_s = \frac{1 - \mu_s^2}{\frac{1}{E_a} - \frac{(1 - \mu_I^2)}{E_I}}, \quad (4)$$

with $\mu_s = 0.2$ and $\mu_I = 0.2$ being Poisson's ratios of the sample and indenter respectively, and $E_I = 614$ GPa, the elastic modulus of the indenter. For the load range

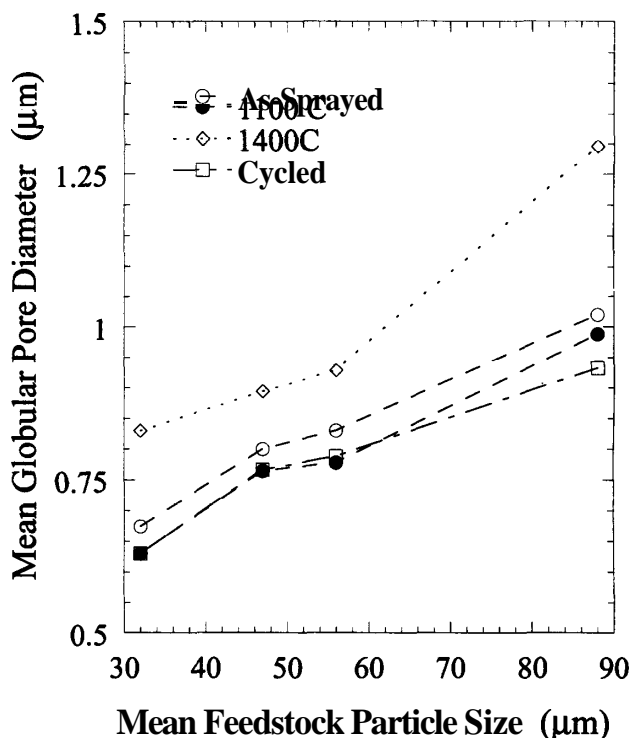


FIG. 7. The diameter of the globular pores, as determined from the 3-component void model, is shown as a function of the mean size of the feedstock powder at different annealing temperatures. The broken lines are guides for the eyes.

examined here, it was found that $E_a^{2/3}$ versus h was linear, indicating an elastic behavior of the deposits. In Table IV, we list the values of the components of the modulus for the deposits made with ensemble and coarse feedstocks.

In Fig. 8 both components of the elastic modulus are plotted as a function of the annealing temperature for the samples sprayed with ensemble and coarse feedstocks. It is clear that because of the structural anisotropy in the samples there is a difference in the components of measured elastic modulus along the two orientations. Moreover, this difference between samples increases with the annealing temperature. A correlation would be expected between the changes in the elastic modulus and those of the internal surface area and/or the porosity. To establish which correlation applies, the variations of the mean

elastic modulus $E_m = (E_{\parallel}E_{\perp}^2)^{1/3}$ are plotted as a function of the total porosity and the internal surface area in Figs. 9(a) and 9(b), respectively. The modest changes in the porosity and internal surface area that occur due to thermal annealing clearly cause significant change in the mean elastic modulus. Figure 9(b) indicates the possible existence of a simple relation between the changes of the internal surface area and the mean elastic modulus. Although the measurements are obtained from two samples with very different porosities, the data appear to fall onto the same curve. In contrast, there is no obvious relation between the mean elastic modulus and porosity itself, when the feedstock particle size is changed. This result corroborates earlier results reported in Ref. 10.

IV. DISCUSSION

It is first important to mention that the strong and measurable MSANS broadening anisotropy was the key factor in analyzing the microstructure of the present samples. Together with the measured total porosity and the total internal surface area (Figs. 2 and 4), the two sets of MSANS-broadening data (one obtained with incident beam direction parallel to the symmetric axis and the other obtained with the incident beam direction perpendicular to the symmetric axis) were required to calculate the volume fractions, characterize the morphology, and determine the angular orientations of the main void-components. Here, a 3-component void model was used to fit and analyze the two sets of data.⁵ This model is simple and reliably captures the essential characteristics of the complex microstructure. A few remarks should be made, however, about the validity and limitations of the model as well as the resulting fit of the MSANS broadening data.

The size R_0 , shown in Fig. 7, is exact within the context of the model but should not be taken as an absolute measurement of the sizes of the actual pores. Indeed, SEM images show significant variations in the size of the various pores of the actual microstructure of the deposits. So R_0 represents a typical size of the porous medium, which is in the micrometer range, close to the size range observed in SEM images. More specifically, $2\beta_1R_1$ and $2\beta_2R_2$ (or $2/3$ of these values) represent the maximum (or mean) opening dimension of the intrasplat cracks and interlamellar pores, respectively, while $2R_0$ is a measure of the globular pore diameter.⁹ It is much more interesting and insightful, however, to consider the trend of the changes of R_0 as a function of the mean size of the feedstock under different heat-treatment conditions (Fig. 7). Here we note that the diameter $2R_0$ increases as a function of the mean size of the feedstock. As generally known, coarser feedstock powder tends to yield more porous deposits under similar spray conditions, possibly because of looser intersplat contacts. Heat treatment induces a monotonic increase in the spacing between the

TABLE IV. Values of the components of elastic modulus measured along the axis parallel to the spray direction (E_{\parallel}) and along one of the axis perpendicular to the spray direction (E_{\perp}) of the deposits made with the ensemble and the coarse feedstock Metco powders.

| Sample | Temperature (°C) | E_{\perp} (GPa) | E_{\parallel} (GPa) | E_{\parallel}/E_{\perp} |
|----------|------------------|-------------------|-----------------------|---------------------------|
| Coarse | as-sprayed | 20.98 ± 1.32 | 10.32 ± 0.78 | 0.49 |
| Coarse | 1100 | 39.51 ± 2.24 | 12.32 ± 1.70 | 0.31 |
| Coarse | 1400 | 68.84 ± 4.76 | 35.88 ± 4.46 | 0.52 |
| Ensemble | as-sprayed | 31.71 ± 1.17 | 16.46 ± 1.25 | 0.52 |
| Ensemble | 1100 | 50.85 ± 4.28 | 22.81 ± 2.02 | 0.45 |
| Ensemble | 1400 | 80.18 ± 4.12 | 52.57 ± 3.19 | 0.65 |

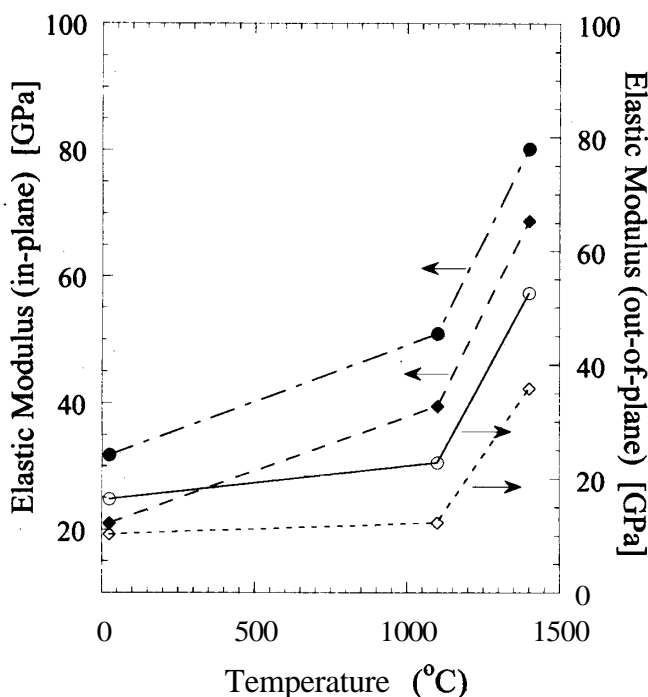


FIG. 8. Measured elastic modulus components of the deposits made from the ensemble (open and full circles) and the coarse (open and full diamonds) feedstock powders are plotted against the annealed temperature.

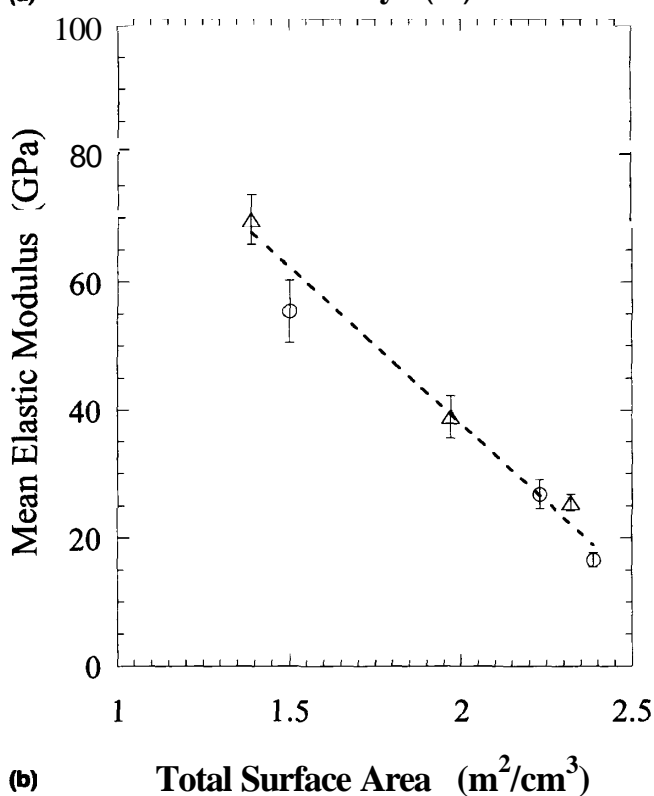
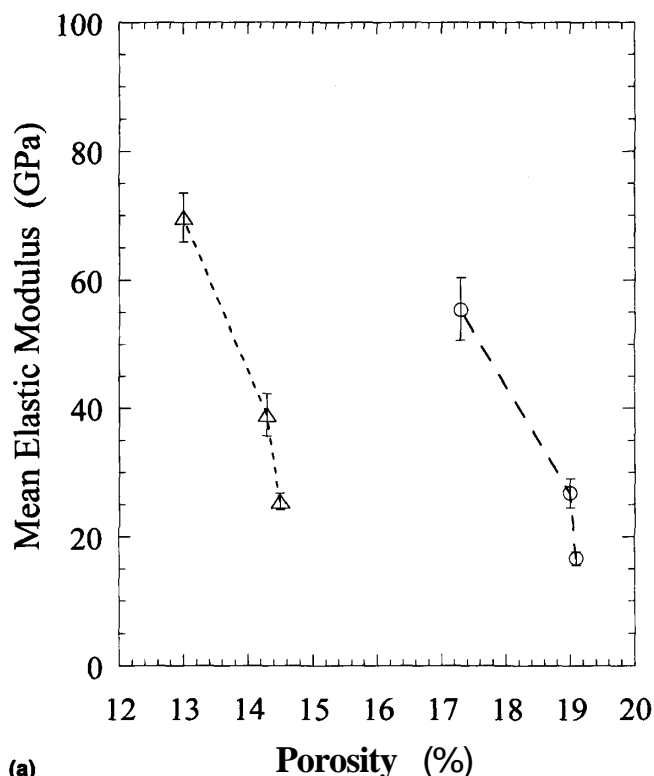


FIG. 9. The mean elastic modulus of the deposits made with the ensemble (A) and the coarse (O) feedstock powders is shown as a function of (a) the measured total porosity and (b) the total surface area. The error bars are two standard uncertainties in length determined from the measurements. The lines in (a) are guides for the eyes, while that in (b) is determined from a weighted least-squares fit of the data to a linear function.

splats; R_0 increases as a function of the annealing temperature. Although not presented in this paper, the SEM images confirm these results.

Comparison of the calculated and measured anisotropy in the MSANS data shows reasonable agreement (Fig. 6). However, it is not, in general, possible to use the 3-void MSANS model to reconstruct the anisotropic Porod surface variation [Fig. 3(c)]. As has been discussed elsewhere,⁹ Porod scattering greatly amplifies the true microstructure anisotropy and can be very sensitive to the details of the shape of the individual scattering features. For example, for oblate spheroidal scatterers, monodisperse in size, orientation, and shape, and with aspect ratio β , the predicted Porod scattering anisotropy is $1/\beta^4$. Thus, for anisotropic Porod surface analysis, the MSANS model microstructure is an oversimplification of the actual disordered microstructure, and it cannot be expected (usually) to provide a successful reconstruction of the observed Porod scattering. The MSANS broadening is generally less sensitive to the β -ratios derived from the data analysis.^{5,9} Thus, our efforts focused on fitting the MSANS anisotropy by finding appropriate internal proportions of the void components.

The total porosity and the total internal surface area curves in Figs. 2 and 4 display a smooth behavior as a function of the mean feedstock size of the particle powder. Interestingly, the behavior of the sample made from as-received powder (ensemble) is no different from the rest of the samples despite its wider feedstock particle size distribution (see Table I). This suggests that the size distribution of the powder does not induce significant variations in the microstructure of the deposit if the processing parameters are well controlled.

The sample made with coarse feedstock powder (88 μm) stands out with its relatively large porosity ($\approx 19\%$), which is 30% more than that of the other samples (13–14%). However, comparison of the total internal surface areas shows that variation in S_v does not exceed 15% among the samples. Application of the 3-void model shows that the large porosity in the deposit made with coarse feedstock powder results from a less efficient packing of the splats during spraying, characterized by a large globular pore radius R_0 for this sample (see Fig. 7). As Fig. 2 suggests, it appears that this observation is general. That is, increasing the size of the feedstock powder increases the porosity of the deposit.

In general, heat treatment yields a decrease in both the porosity and the specific surface area of all the samples. Analysis with the 3-void model shows first that annealing causes a mild coarsening of the voids at the highest temperature. While the intersplat voids and globular pores together contribute the most to the total porosity ($\geq 95\%$), a reverse occurs here in their relative contributions during annealing (Fig. 2); the globular pores be-

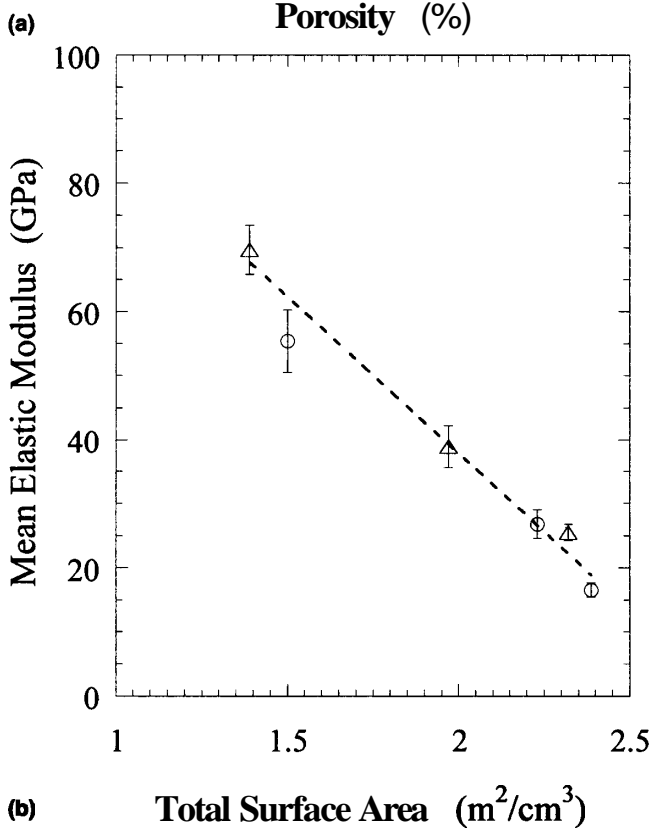
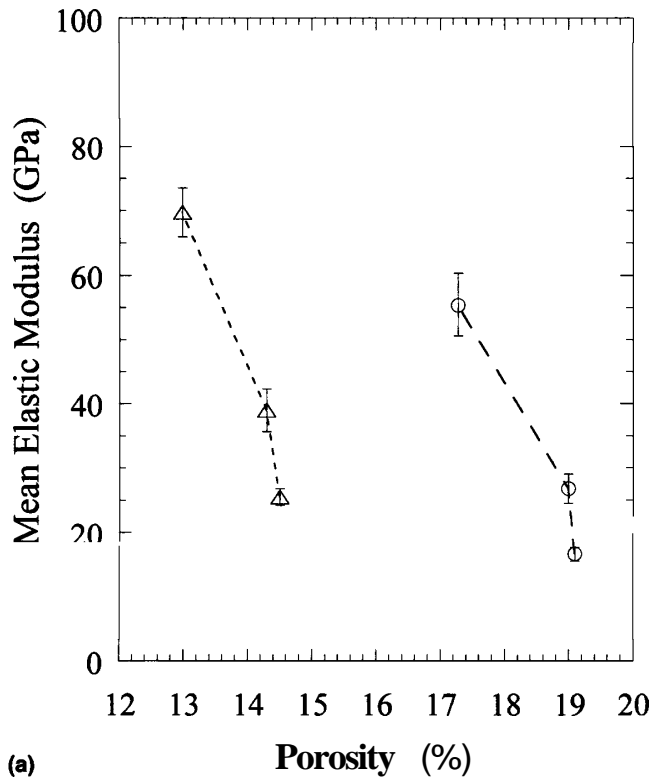


FIG. 9. The mean elastic modulus of the deposits made with the ensemble (A) and the coarse (O) feedstock powders is shown as a function of (a) the measured total porosity and (b) the total surface area. The error bars are two standard uncertainties in length determined from the measurements. The lines in (a) are guides for the eyes, while that in (b) is determined from a weighted least-squares fit of the data to a linear function.

splats; R_0 increases as a function of the annealing temperature. Although not presented in this paper, the SEM images confirm these results.

Comparison of the calculated and measured anisotropy in the MSANS data shows reasonable agreement (Fig. 6). However, it is not, in general, possible to use the 3-void MSANS model to reconstruct the anisotropic Porod surface variation [Fig. 3(c)]. As has been discussed elsewhere, Porod scattering greatly amplifies the true microstructure anisotropy and can be very sensitive to the details of the shape of the individual scattering features. For example, for oblate spheroidal scatterers, monodisperse in size, orientation, and shape, and with aspect ratio β , the predicted Porod scattering anisotropy is $1/\beta^4$. Thus, for anisotropic Porod surface analysis, the MSANS model microstructure is an oversimplification of the actual disordered microstructure, and it cannot be expected (usually) to provide a successful reconstruction of the observed Porod scattering. The MSANS broadening is generally less sensitive to the β -ratios derived from the data analysis.^{5,9} Thus, our efforts focused on fitting the MSANS anisotropy by finding appropriate internal proportions of the void components.

The total porosity and the total internal surface area curves in Figs. 2 and 4 display a smooth behavior as a function of the mean feedstock size of the particle powder. Interestingly, the behavior of the sample made from as-received powder (ensemble) is no different from the rest of the samples despite its wider feedstock particle size distribution (see Table I). This suggests that the size distribution of the powder does not induce significant variations in the microstructure of the deposit if the processing parameters are well controlled.

The sample made with coarse feedstock powder (88 μm) stands out with its relatively large porosity ($\approx 19\%$), which is 30% more than that of the other samples (13–14%). However, comparison of the total internal surface areas shows that variation in S_v does not exceed 15% among the samples. Application of the 3-void model shows that the large porosity in the deposit made with coarse feedstock powder results from a less efficient packing of the splats during spraying, characterized by a large globular pore radius R_0 for this sample (see Fig. 7). As Fig. 2 suggests, it appears that this observation is general. That is, increasing the size of the feedstock powder increases the porosity of the deposit.

In general, heat treatment yields a decrease in both the porosity and the specific surface area of all the samples. Analysis with the 3-void model shows first that annealing causes a mild coarsening of the voids at the highest temperature. While the intersplat voids and globular pores together contribute the most to the total porosity ($\geq 95\%$), a reverse occurs here in their relative contributions during annealing (Fig. 2); the globular pores be-

come the dominant volume contributor for higher annealing temperatures. This trend can be attributed to the coarsening and reshaping of some of the cracks at high temperatures, thereby increasing the volume fraction of the globular pores. However, since the process depends on the relative initial populations of globular pores, interlamellar voids, and cracks, a different feedstock morphology with fewer cracks might not show such a reverse in the relative contributions of globular pores and intersplat voids.

The internal surface area from the intersplat voids represents the most sizable proportion of the total internal surface area (Fig. 4), even after annealing. However, the small contribution from the globular pores in the as-sprayed condition becomes more significant than that of the cracks upon annealing. Note that the 1-h heat treatments do not anneal out the cracks completely, even at the highest temperature, 1400 °C. A longer annealing time may be needed. Further, annealing of the cracks should not be expected to affect significantly the microstructural anisotropy of the deposits. In fact an increase in the observed anisotropy might be expected since the annealing cracks, which are preferentially oriented perpendicular to the substrate, will contribute less to the scattering. In contrast, the persisting intersplat voids remain preferentially oriented parallel to the substrate and should give rise to an overall increase of the anisotropy. The SANS measurements confirm this prediction.

Up to 1100 °C, there are no observable differences in the microstructure of the samples heat treated by a single thermal cycle and those that were thermal cycled several times. Initially, thermal cycling was expected to have a cumulative effect on the annealing process, thereby causing additional changes in the microstructure. Our measurements, however, do not indicate so. This result cannot be generalized, however, to all temperatures; at 1400 °C a phase transformation may occur,¹² and thermal cycling might then show a cumulative effect on the deposit.

The indentation measurements showed that the elastic modulus increases as a function of annealing temperature along both the spray direction and parallel to the substrate. This observation should be expected, given that the porosity decreases during annealing. The anisotropic nature of these deposits shows up in the values of the elastic modulus measured along the two different directions. An interesting goal is to find a simple relationship between the sample component porosities and the elastic modulus of anisotropic composites, such as the present deposits. At this time, it is unclear how such an accurate relationship should be formulated, although an approach along the lines of that proposed in Ref. 13 seems likely.

In summary, changing the size of the feedstock powder does not induce dramatic changes in the microstructure of the deposits, whether or not all the particles melt

during the spray process. However, while the total internal surface area remains almost constant, the total porosity increases monotonically with feedstock particle size. This is perhaps one of the more interesting findings of our study. Unfortunately, while a simple, perhaps universal, result is suggested, the complex heterogeneous nature of the coatings means that a number of complicated processes may be superimposed on one other. Thus, further study of the various possible influences on particle subpopulations differentiated by shape, composition, and detailed morphology, as well as by size, would be fruitful. Heat treatments induce changes in the microstructure, but these changes follow a similar trend for all the deposits. Generally, a monotonic variation in the microstructural parameters with feedstock particle size remains after annealing. This monotonic dependence extends to the as-received powder, which has a much broader particle size distribution (encompassing all the others). This suggests that the feedstock mean particle size may be a useful process control parameter in designing better optimized deposit microstructures but that the detailed particle size distribution may not play a significant role especially if the spray process melts all of the particles.

ACKNOWLEDGMENT

Certain trade names and company products are identified to adequately specify the experimental procedure. In no case does such identification imply recommendation or endorsement by the National Institute of Standards and Technology; nor does it imply that the products are necessarily the best for the purpose.

REFERENCES

1. J. Ilavsky, A.J. Allen, G.G. Long, S. Krueger, C.C. Berndt, and H. Herman, *J. Am. Ceram. Soc.* **80**, 733 (1997).
2. G. Porod, in *Small-Angle X-ray Scattering*, edited by O. Glatter and O. Kratky (Academy Press, London, U.K., 1982), pp. 17–51.
3. G. Kostorz, *Neutron Scattering* (Academic Press, New York, 1979).
4. J. Ilavsky, A.J. Allen, G.G. Long, S. Krueger, H. Herman, C.C. Berndt, and A.N. Goland, in *Thermal Spraying-Current Status and Future Trends*, edited by A. Ohmori (High Temperature Society of Japan, Osaka, Japan, 1995), pp. 483–488.
5. A.J. Allen, J. Ilavsky, G.G. Long, J.S. Wallace, C.C. Berndt, and H. Herman, *Acta Mater.* **49**, 1661 (2001).
6. C.J. Glinka, J.M. Rowe, and J.G. LaRock, *J. Appl. Crystallogr.* **19**, 427 (1985).
7. N.F. Berk and K.A. Hardman-Rhyne, *J. Appl. Crystallogr.* **18**, 467 (1985).
8. K.A. Hardman-Rhyne and N.F. Berk, *J. Appl. Crystallogr.* **18**, 473 (1985).
9. A.J. Allen and N.F. Berk, *J. Appl. Crystallogr.* **27**, 878 (1994).
10. J.S. Wallace and J. Ilavsky, in *Thermal Spray: A United Forum for Scientific and Technological Advances*, edited by C.C. Berndt (ASM International, Materials Park, OH, 1997), pp. 757–762.
11. W.C. Oliver and G.M. Pharr, *J. Mater. Res.* **7**, 1564 (1992).
12. J. Ilavsky and J.K. Stalick, *Surf. Coat. Technol.* **127**, 120 (2000).
13. I. Sevostianov and M. Kachanov, *Acta Mater.* **48**, 1361 (2000).